Microfluidics in structured multimaterial fibers

Rodger Yuan[a], Jaemyon Lee[b,c,d], Hao-Wei Su[b,c,d], Etgar Levy[c], Tural Khudiyev[c], Joel Voldman[b,c,d,1], and Yoel Fink[a,c,1]

[a]Department of Materials Science and Engineering, Massachusetts Institute of Technology, Cambridge, MA 02139; [b]Department of Electrical Engineering and Computer Science, Massachusetts Institute of Technology, Cambridge, MA 02139; [c]Research Laboratory of Electronics, Massachusetts Institute of Technology, Cambridge, MA 02139; and [d]Microsystems Technology Laboratories, Massachusetts Institute of Technology, Cambridge, MA 02139

Edited by John A. Rogers, Northwestern University, Evanston, IL, and approved September 18, 2018 (received for review June 1, 2018)

Traditional fabrication techniques for microfluidic devices utilize a planar chip format that possesses limited control over the geometry of and materials placement around microchannel cross-sections. This imposes restrictions on the design of flow fields and external forces (electric, magnetic, piezoelectric, etc.) that can be imposed onto fluids and particles. Here we report a method of fabricating microfluidic channels with complex cross-sections. A scaled-up version of a microchannel is dimensionally reduced through a thermal drawing process, enabling the fabrication of meters-long microfluidic fibers with nonrectangular cross-sectional shapes, such as crosses, five-pointed stars, and crescents. In addition, by codrawing compatible materials, conductive domains can be integrated at arbitrary locations along channel walls. We validate this technology by studying unexplored regimes in hydrodynamic flow and by designing a high-throughput cell separation device. By enabling these degrees of freedom in microfluidic device design, fiber microfluidics provides a method to create microchannel designs that are inaccessible using planar techniques.

fibers | microfluidics | interial focusing | dielectrophoresis | fabrication

Over the past few decades, microfluidics has become an established platform for the development of new methods and devices in the life sciences and chemistry (1–5). Top-down fabrication approaches for microfluidic devices—whether via planar processing (6), soft lithography (7), injection molding (8), etc.—almost always result in the creation of 2D extruded structures with rectangular cross-sections. These planar processes are restricted in their ability to create enclosed channels with arbitrary cross-sections and to exceed the size of the underlying silicon wafer. In addition, it is not possible to arbitrarily position nonstructural elements, such as conductive electrodes, which are key design considerations in many microfluidic applications (9–11). While it has been shown that nonrectangular channels can enhance microfluidic device performance (12–16), the exploration of complex cross-sectional geometries has been limited.

In this article, we introduce fiber microfluidics, an approach that circumvents many of the limitations of existing fabrication processes by leveraging dimensional reduction to create complex microchannels that are uniform over arbitrary lengths. The basis of fiber microfluidics is the thermal fiber drawing technique, in which a scaled-up version of the fiber (i.e., the preform) is heated and drawn, resulting in cross-sectional reduction while maintaining cross-sectional geometry (Fig. 1*A*). This enables the fabrication of useful microfeatures, such as precisely shaped and multimaterial channels with uniformity over meter-length scales that are largely inaccessible by other fabrication processes. The fiber microfluidic platform aims to bring three primary advantages over traditional photolithographic approaches: (*i*) unrestricted device length; (*ii*) complete design freedom over cross-sectional microchannel geometry, or geometric cross-sectional tunability; and (*iii*) unrestricted cross-sectional material positioning of functional elements, or multimaterial functionality.

We present the utility of the fiber microfluidics system in the context of particle manipulation and separation. First, we developed a method to fabricate channels with arbitrary cross-sectional shape to study inertial particle focusing in straight channels with complex features. Then, we utilize this understanding of inertial focusing behavior in complex-shaped channels to design and fabricate an optimized inertial-dielectrophoretic (DEP) particle manipulation fiber (Fig. 1*B*) that, in conjunction with a 3D-printed self-aligning fiber-to-world connection, can perform sheathless live and dead cell separation at 100 μL min^{-1}.

Results

Geometric Cross-Sectional Tunability: Inertial Microfluidics. First, we used geometric cross-sectional tunability to probe regimes in inertial microfluidics. Inertial microfluidics is the study of microparticle focusing and separation in laminar flow regimes which require the inclusion of the inertial terms in the Navier–Stokes equation to accurately describe particle behavior (17). In straight, rectangular channels, particles have been found to migrate to predictable equilibrium positions based on the channel cross-section (18, 19), which have been used as passive methods for high-throughput particle focusing (20, 21) and separation (22, 23). While the spatial location of inertial focusing positions in primary flows is highly dependent on its cross-sectional geometry, fabrication challenges have limited experimental study to only simple shapes [rectangles (18, 24), circles (25), triangles (15)]. Thus, applications that utilize primary inertial forces are designed with limited control over the spatial location of focusing positions along the cross-section.

We developed a preform molding method that enables the fabrication of microchannels with arbitrary geometry (*SI Appendix*, Fig. S1). We fabricated two complex channel shapes: an

Significance

The development of microfluidics, or the study of fluid behavior and manipulation at the microscale, has largely been catalyzed by microfabrication techniques based on a planar chip format. While immensely powerful, planar fabrication methods have inherent restrictions that prevent the realization of relatively simple channel structures, such as nonrectangular cross-sectional geometries and arbitrary cross-sectional materials placement. This study introduces a microfluidics fabrication method based on a fiber format that enables the construction of microchannels with highly tunable cross-sectional geometries and a broad range of materials. This approach allows for degrees of freedom in the design and function of microfluidic systems, thereby extending the reach of realizable microfluidic devices.

Author contributions: R.Y., J.L., H.-W.S., J.V., and Y.F. designed research; R.Y., J.L., and T.K. performed research; R.Y., J.L., H.-W.S., and E.L. contributed new reagents/analytic tools; R.Y. and J.L. analyzed data; and R.Y. wrote the paper.

The authors declare no conflict of interest.

This article is a PNAS Direct Submission.

[1]To whom correspondence may be addressed. Email: voldman@mit.edu or yoel@mit.edu.

This article contains supporting information online at www.pnas.org/lookup/suppl/doi:10.1073/pnas.1809459115/-/DCSupplemental.

Published online October 29, 2018.

equilateral cross-shaped channel and a star-shaped channel (Fig. 2 *A* and *B*), each with a maximum channel dimension of 125 μm. Particle distributions within the fibers were observed for 10-μm fluorescent polystyrene beads suspended in water flowed over a range of particle Reynolds numbers [R_p, defined as $R_p = Re(a/H)^2 = \rho U a^2/\mu H$, where ρ is the fluid density, U is the maximum fluid velocity, a is the particle diameter, μ is the fluid viscosity, and H is the hydraulic diameter of the channel].

Long exposure fluorescence (LEF) streaks of polystyrene beads focused through the cross-shaped channel at R_p = 0.1 demonstrate stronger focusing with increasing device length (Fig. 2*C*). This is a result of the linear relationship between particle residency time and length of the device. This is important to emphasize because our fiber drawing process is capable of drawing devices of arbitrary length, allowing for longer particle residency times and therefore higher flow rates.

Within the cross-shaped channel, LEF streaks (Fig. 3*A*, *Left*) show that inertial lift forces are significant in flows of particle Reynolds numbers as low as 0.17, where particles are weakly focused into two streaks along the center third of the cross. Furthermore, as the particle Reynolds number of the flow increases, peaks become sharper as particles are more strongly focused into their equilibrium positions.

We can deduce by symmetry from the LEF images that there are four equilibrium migration positions along the channel cross-section (Fig. 3*A*, *Center Right*); two are represented by the two streaks present in the LEF image and the other two are directly beneath them in the –*y* direction, obstructed from view. We confirmed this by imaging the *x*-*y* plane of the microchannel using fluorescence confocal microscopy (Fig. 3*A*, *Right*), which also shows four distinct equilibrium positions in agreement with those predicted from LEF.

We further studied the influence of concave geometric features on inertial focusing positions using a five-pointed star channel (Fig. 3*B*). To our knowledge, fabrication of such a microchannel has not been demonstrated using traditional microfabrication approaches. The LEF images (Fig. 3*B*, *Center Left*) from the star channel show that particles migrate to three streaks at the center of the channel that sharpen as the particle Reynolds number increases. From the fivefold symmetry of the star shape, we are able to deduce that there are five inertial focusing positions for the star geometry, also located adjacent to each of the five concave corners of the star. When R_p reaches 2.87, additional shoulder peaks emerge along the inner sides of the outer streaks. These peaks represent the upper two equilibrium positions shown in Fig. 3*B* (*Center Right*), which are overlapped into a single streak at lower R_p where the inertial lift forces are weaker. Confocal microscopy of the *x*-*y* plane (Fig. 3*B*, *Right*) confirmed the positions of the five equilibrium points.

Mechanisms of Particle Migration. We used numerical modeling to calculate the inertial lift forces along the cross-section of each microchannel (Fig. 4 *A* and *B*). The method of numerical modeling is outlined in Di Carlo et al. (18). In the force plots for both the equilateral cross and star, there exist two equilibrium points: one stable position near the concave corner along the short axis (SA, blue line) that runs from the channel center to a concave corner and one unstable position far from the center along the long axis (LA, green line) that runs from the channel center to the midpoint of an extremity.

The inertial force plots show two general trends: (*i*) particles moving along the LA in the +*y* direction are drawn away from the channel center and (*ii*) particles off of the LA are guided in a two-step process in which they first move away from the channel

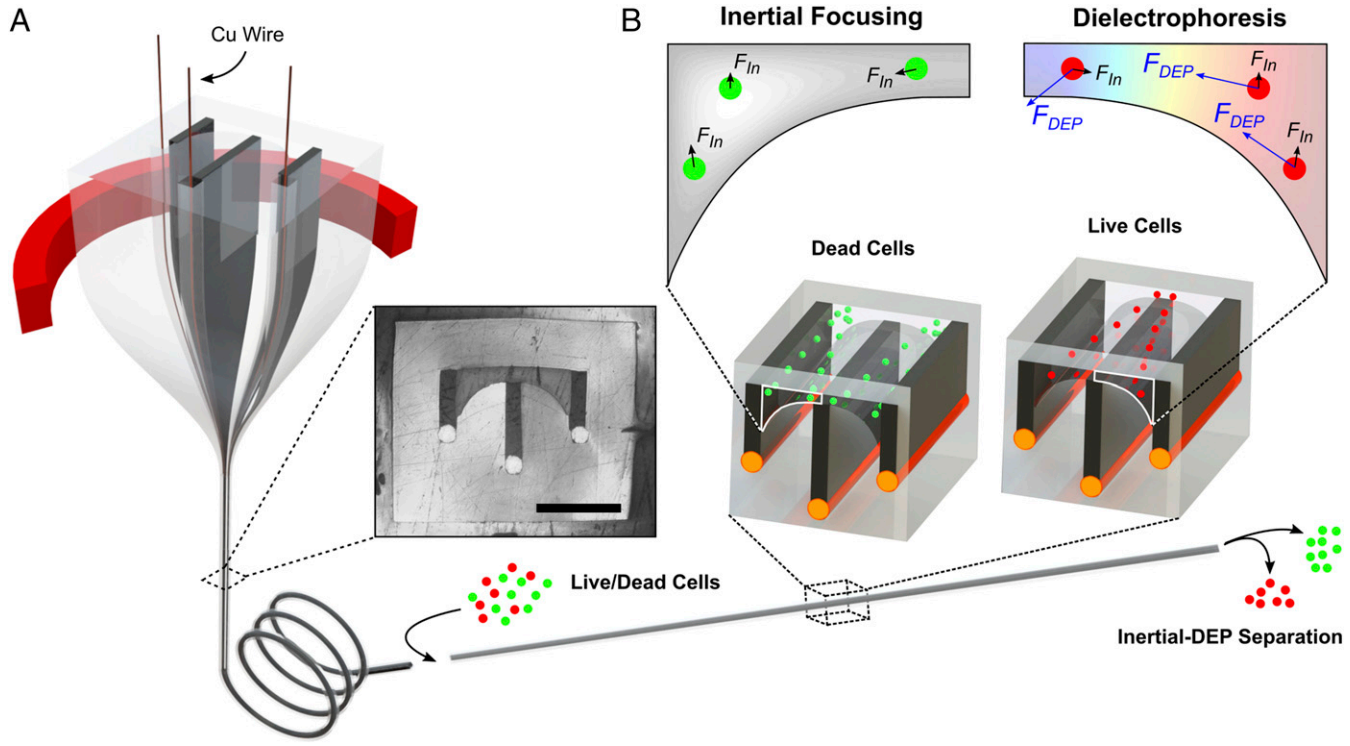

Fig. 1. Multimaterial fiber fabrication and design. (*A*) A schematic of the thermal drawing process showing a preform being fed through the hot zone (red ring) and drawn into a fiber with cofeeds of copper wire. The fiber cross-section (*Inset*) matches that of the preform. (Black scale bar: 200 μm.) (*B*, *Bottom*) Live and dead cells are flowed through the fiber and subjected to different magnitudes of inertial (*Left*) and dielectrophoretic (*Right*) forces, which result in particle migration to different positions within the fiber.

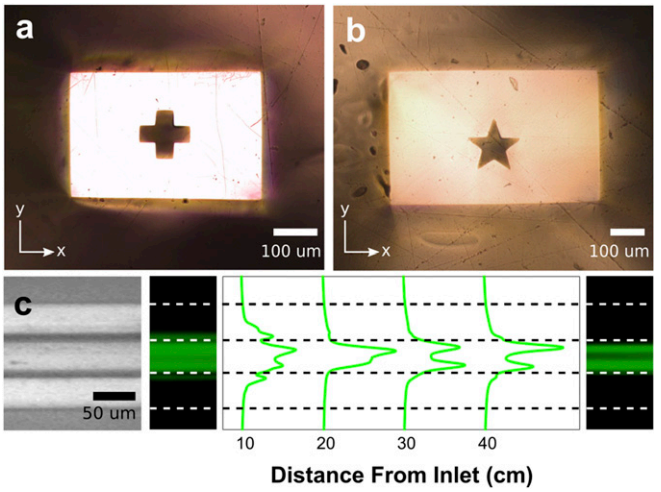

Fig. 2. High-aspect-ratio microchannels with structurally complex cross-sections. (*A* and *B*) Cross-sectional images of the cross-shaped and star-shaped channels. (*C*) LEF images of polystyrene particle focusing within a cross-shaped fiber at $R_p = 0.1$ at various distances from the bead inlet.

center in the $+x$ direction and then in the $-y$ direction until they reach the stable equilibrium position.

While the focusing behavior of the equilateral cross and star channels is unprecedented, the effect of concave geometric features on inertial equilibrium positions is consistent with prevailing knowledge on inertial particle migration. Inertial lift is dominated by two opposing forces: the shear-gradient lift force, which acts in the opposite direction of the shear gradient and typically directs particles to walls, and the wall-induced lift force, which directs particles away from the channel walls. Equilibrium points arise when the sum of these two forces is equal from all directions.

The focusing behavior of the equilateral cross and star channel is caused by a high shear-gradient lift force along the SA relative to that of the long LA. It is widely accepted that the shear-gradient lift force is strongly dependent on the magnitude of the shear rate (17, 26). The concave corner creates a shear-rate asymmetry in which the shear rate along the SA is greater than that along the LA (Fig. 4 *C* and *D*). In analogy with previous works describing inertial equilibrium positions in rectangular channels (19, 24), this causes particles destabilized off of the LA to migrate in the $+x$ direction under dominant shear-gradient lift force until they are directed toward the stable equilibrium point on the SA by dominant wall-induced lift forces. The origin of this asymmetry can be seen from the simulated velocity profiles shown in Fig. 4*E*, which shows the axial velocity of a fluid flowing in a particleless channel with no-slip boundary conditions. The maximum axial velocity is located at the origin, so the shear gradient will be greater along the SA relative to the LA because the distance from the channel center to the wall is shorter.

From this analysis we can see that inertial forces in the equilateral cross and star channels will tend to direct particles to focusing positions along the axes between the channel center and concave corners because of the effect of concave corners on the velocity profile of the flow. In short, particles tend to focus along axes that minimize the distance between the location of maximum flow rate and a channel boundary. This general principle is translatable to different geometries, and is especially useful for predicting interial focusing positions in straight channels when considering the large amount of computing power required to perform 3D simulations of inertial flow. With geometric tunability of the fiber microfluidic platform, in conjunction with a growing understanding of inertial behavior, channels can be fabricated to have inertial focusing positions tailored to the need of the particle manipulation applications.

Multimaterial Functionality: Inertial-DEP Cell Separation. To demonstrate the multimaterial functionality of the fiber microfluidics, we introduced conductive materials onto microchannel surfaces to create a sheathless inertial-DEP cell separation device. DEP is an electrokinetic particle manipulation technique that describes the motion of polarizable particles within a nonuniform electric field. Based on the polarizability of the particle relative to the media, particles will move to (pDEP) or away from (nDEP) regions of high electric field strength. DEP is a label-free and specific particle manipulation technique that has been studied for the characterization (27–29), separation (30–33), and trapping (34, 35) of bioparticles.

The fabrication process of planar metal electrodes typically involves metal deposition onto a substrate, photoresist patterning, etching, and bonding to a separate component that includes the microchannels. Because this is a multicomponent process in which electrodes are localized to substrate surfaces, electrode placement is typically restricted to two opposing walls within rectangular channels. The design of nonuniform electric fields within DEP devices with restrictions in both channel geometry and electrode placement result are not ideal for particle manipulation and separation. For example, a common reason for limitations in throughput for DEP devices is that the direction of the DEP force is often perpendicular to the desired direction of particle movement (33, 35, 36). While many studies have explored the use of nonrectangular channel shapes (13) and out-of-plane electrode placement (37), these require complex fabrication techniques and lack the flexibility to design optimized DEP fields.

In contrast to microfabrication techniques, we developed a method that creates a fully integrated DEP microchannel in which electrodes may theoretically be placed at arbitrary positions around an arbitrarily shaped microchannel, enabling additional degrees of freedom in the design of in-channel electric fields. We utilized this capability to design and optimize a microchannel architecture that leverages both inertial forces and DEP forces in tandem to perform sheathless separation of live and dead cells at high throughput.

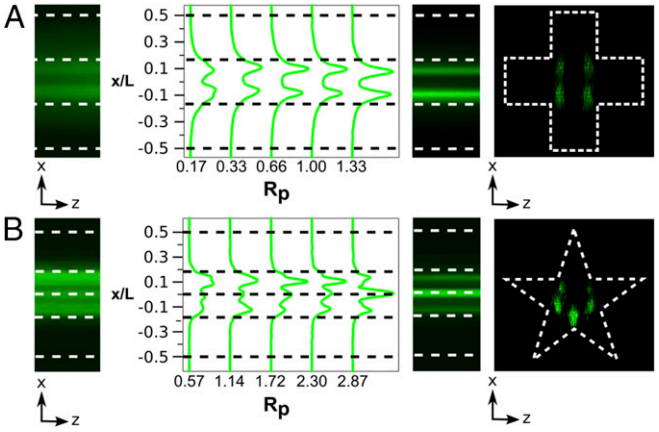

Fig. 3. Inertial focusing characterization in complex microchannels for (*A*) the equilateral cross channel and (*B*) the star channel. LEF images of particle focusing for a range of R_p are analyzed to obtain intensity profiles (*Center Left*) of flowing polystyrene beads (green) relative to the channel walls (white dotted lines) which, through symmetry, are used to deduce the complete set of focusing positions along the cross-section (*Center Right*). Confocal imaging (*Right*) is used to verify the equilibrium positions. The dotted lines for all LEF images represent corners of the channel.

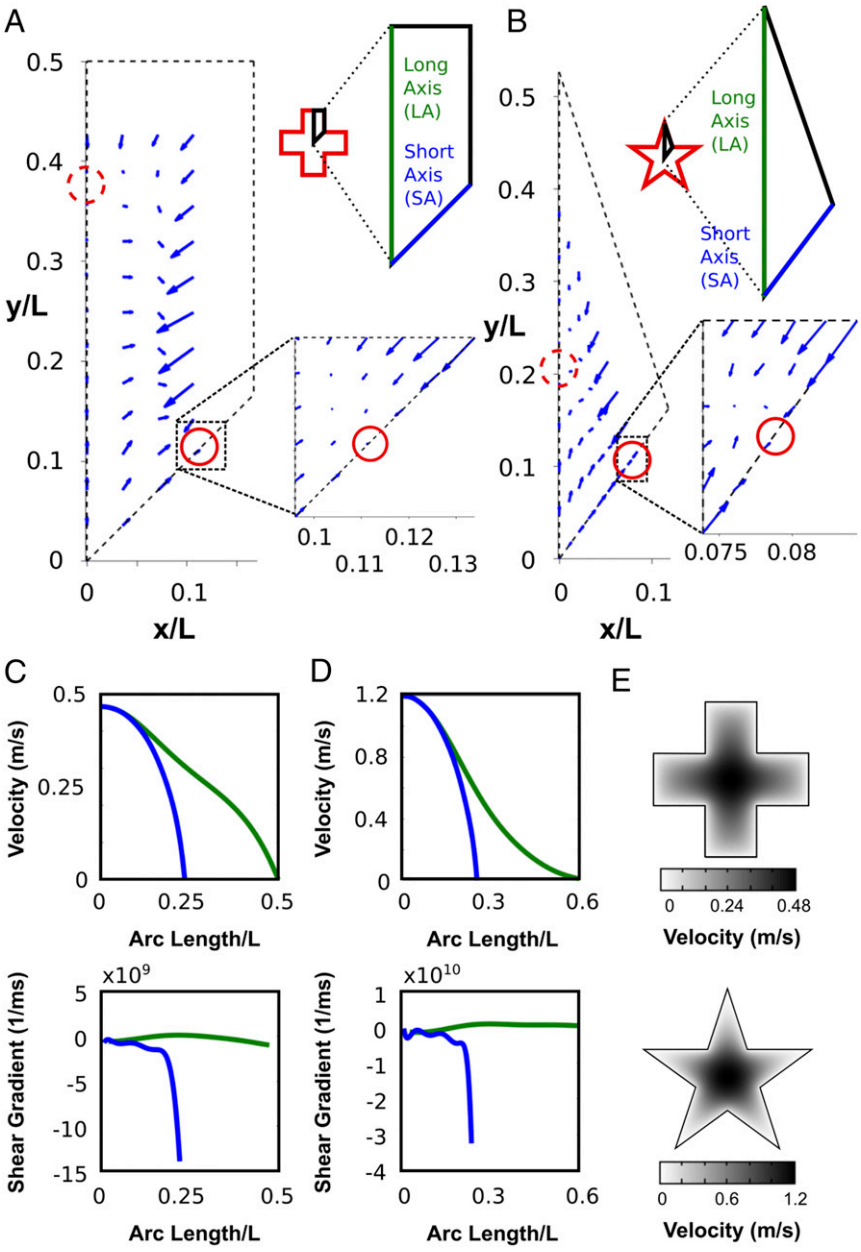

Fig. 4. Numerical modeling of inertial focusing fibers. (*A* and *B*) Vector plot of numerically computed inertial lift forces along a symmetric section of the channel cross-section for the (*A*) equilateral cross-fiber ($R_p = 0.66$) and (*B*) star-shaped fiber ($R_p = 2.3$). Unstable (dotted) and stable (solid) equilibrium positions are indicated by red circles. (*Upper Right, Insets*) Schematics showing the long axis and short axis of a unit cell for each cross-section. (*C* and *D*) Plots of the fluid velocity magnitude (*Top*) and shear-gradient magnitude (*Bottom*) vs. normalized arc length along the LA (green) and SA (blue) for the cross (*C*) and star (*D*) channel under the same flow conditions as *A* and *B*. (*E*) Numerically computed velocity magnitude for the (*Top*) equilateral cross-fiber and (*Bottom*) star-shaped fiber, plotted in grayscale with increasing tint corresponding to increasing velocity, starting from white (velocity = 0) to black (maximum velocity).

Inertial-DEP Fiber Design. Minimizing losses in insulators leads DEP devices to have electrodes in direct contact with the flowing media. Thus, we use conductive polyethylene (CPE), which has a high viscosity at the draw temperature of our cyclic polyolefin copolymer (COC) cladding material, to serve as a conductor–fluid interface material along the interior of the microchannel surface. To minimize axial resistive losses, it was necessary to place a low-resistivity material adjacent to the CPE. Although previous studies have successfully utilized low melting temperature metals in the draw process (38–40), drawing adjacent low-viscosity domains (e.g., liquid metal) frequently leads to kinetic instabilities and dimensional fluctuation (41). Due to the importance of dimensional uniformity on device performance, we developed a zero-tension cofeeding setup that enabled copper wires to be precisely fed into the preform and incorporated into the fiber during the draw. Additional details can be found in *SI Appendix*.

The inertial-DEP cell separation fiber, hereby called the inertial-DEP fiber, was designed with an optimized three-electrode, half-bowtie shape to spatially separate a mixture of pDEP-feeling particles and non-DEP-feeling particles at high throughput (Fig. 5*A*). Both the electric field gradient field and the shear-gradient field were tuned and optimized by adjusting the channel shape and electrode placement. Details of the channel shape design and optimization can be found in *SI Appendix*. In this design, particles experiencing pDEP will be

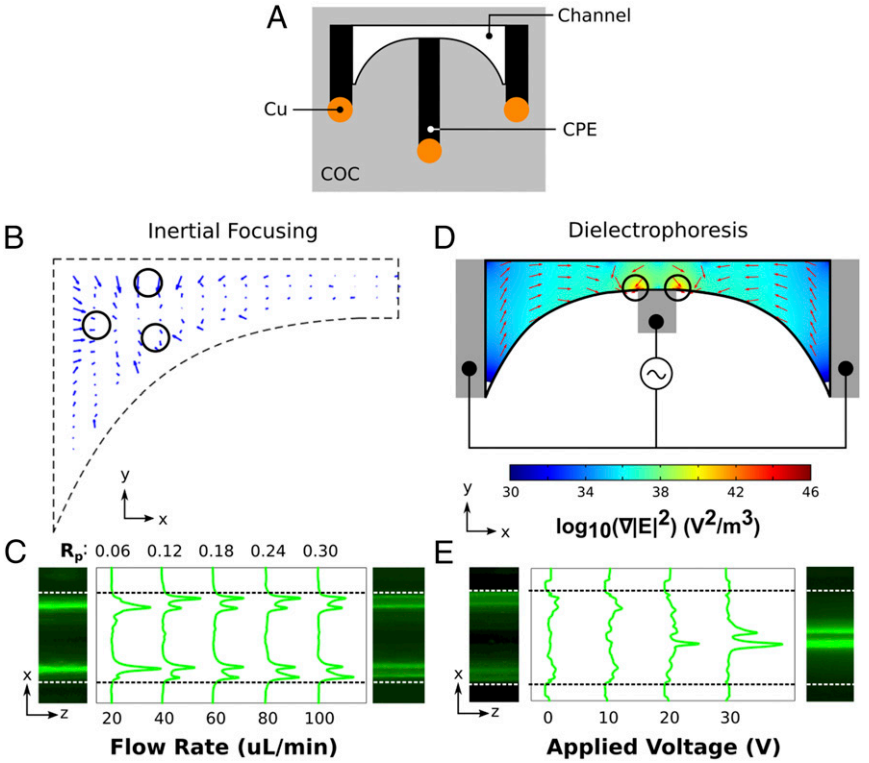

Fig. 5. Inertial-DEP fiber design and characterization. (*A*) Schematic of the cross-section of the inertial-DEP fiber (*B*) Numerically calculated inertial focusing force vectors reveal predicted inertial focusing positions (black circles) at a flow rate of 100 μL min^{-1}. (*C*) LEF images (*Far Left* and *Far Right*) and averaged intensity profiles (*Center*) of polystyrene beads flowed through the fiber at various flow rates. (*D*) Numerically calculated values for the direction and magnitude of log ($\nabla|E|^2$) reveal pDEP focusing positions (black circles) at the corners of the center electrode. (*E*) LEF images (*Far Left* and *Far Right*) and averaged intensity profiles (*Center*) of BA/F3 cells with increasing values of applied voltage. For *C* and *E*, the dotted lines represent the position of the walls of the channel.

focused to the center of the channel through a DEP force, while particles that experience weak DEP forces, which we call weak-DEP particles, will migrate to the edges of the channel via inertial forces. To our knowledge, the thermal drawing-enabled shape and electrode placement of this microfluidic channel cannot be replicated using existing fabrication techniques.

Simulated inertial forces within the half-bowtie channel predict inertial particle focusing toward the edges of the channel (Fig. 5*B*). The in-fiber performance of the inertial-DEP fiber was characterized using LEF along the *x-z* plane of a 75-cm-long fiber. In the absence of applied voltage, 10-μm polystyrene beads were flowed through the channel and were found to exhibit focusing behavior to the outside of the channel at flow rates as low as 20 μL min^{-1} (Fig. 5*C*). Even at low flow rates, where inertial forces are small, the long length of the fiber allows enough residency time to allow for migration toward the equilibrium positions. At 100 μL min^{-1}, the observed inertial focusing positions correspond well to those predicted by simulation.

Fig. 5*D* shows the simulated direction and magnitude of $\nabla|E^2|$, which is proportional to the DEP force, when a 25-V voltage is applied between the outer and center electrodes. The DEP profile reveals focusing positions at the inner tips of the center CPE electrode, as expected. To verify the DEP performance of the fiber, pDEP-experiencing BA/F3 cells suspended in a low-conductivity isoosmotic solution were flowed at a rate of 100 μL min^{-1}. In the absence of voltage, inertial forces migrate cells toward the vertical walls of the channel. It is important to note that the inertial focusing behavior of cells tends to result in a broader particle distribution relative to rigid beads. This observation is consistent with those seen in previous studies (23), and can be attributed to differences in the size distributions of the BA/F3 cells and polystyrene beads, which both had mean diameters of 10 μm and had SDs of 1.8 and 1.0 μm, respectively. Both migration equilibrium position and magnitude of the migration force are functions of the diameter of the particle (19), so the higher-variability cell population results will focus to a wider range of equilibrium positions. In addition, since the magnitude of the migration force scales with $1/a^3$, small particles or cellular debris may not have had sufficient time to reach their equilibrium positions, resulting in a broader distribution.

As predicted by simulation, when the applied voltage is increased to 30 V, the DEP force on the BA/F3 cells is large enough to overcome the inertial forces, and cells migrate to the center of the channel (Fig. 5*E*).

DEP Cell Separation Device. We utilize the inertial-DEP fiber to create a sheathless cell separation device capable of continuous separation of live and dead BA/F3 cells at throughputs as high as 100 μL min^{-1}. To prepare the dead cells, they were fixed using a 10% neutral-buffered formalin solution, after which the cells' DEP response switched to weak nDEP. In the absence of an applied voltage, all cells are focused to the inertial focusing positions of the fiber and spatial separation between cell types is not realized. Under an applied field at 10 MHz, the pDEP live cells feel a DEP force strong enough to overcome the inertial focusing forces and focus to the center of the fiber, while the weak nDEP-feeling dead cells remain in the inertial focusing positions. Movie S1 shows the in-fiber spatial separation of a mixture of live and dead BA/F3 cells suspended in a low-conductivity isoosmotic solution flowed through a 75-cm-long inertial-DEP cell separation fiber at a rate of 100 μL min^{-1}.

For a continuous cell separation device to be useful, cell populations must be physically separated at the outlet, which means splitting the flow from the fiber into multiple outlets. We

designed a 3D-printed fiber-to-world (FTW) connector that can mate with our fibers at the outlet and can transition the flow from the fiber into multiple outlets.

We designed the FTW connector to create a complete cell separation device capable of physically separating live and dead BA/F3 cells at the outlet of the inertial-DEP fiber device. The FTW connector is designed to mate with the fiber outlet without significantly disturbing laminar streamlines and maintain the spatial separation of particles generated by the fiber. The 3D-printed chip consists of three sections: (*i*) a self-aligning mating port, (*ii*) a fiber/FTW interface, and (*iii*) a trifurcation fork (Fig. 6*A*).

The self-aligning mating port was designed such that exterior dimensions of the inertial-DEP fiber were matched with the interior dimensions of the port (Fig. 6 *B* and *C*). In this manner, it is possible to easily align the fiber channel with the interfacing channel within the chip.

At the fiber/FTW interface, the interior channel of the FTW was designed to be 30% wider than the size of the half-bowtie channel to allow for slight errors in the alignment process that arise from limitations in the resolution of the stereolithography 3D printer used. A small semicircle at the bottom of the interior channel was included to match the profile of the fiber to the FTW (Fig. 6*D*).

At the trifurcation fork, a single outlet is split into three separate outlets to physically separate the particles (Fig. 6*E*). Assuming laminar flow is maintained through the fiber/FTW interface, then preservation of in-fiber particle positions within streamlines would facilitate the movement of live cells to the center outlet and dead cells to the outer two outlets (Fig. 7 *A*–*D*).

When the DEP fiber is slotted into the FTW, the center of the top section of the mating channel aligns with the center of the fiber channel. The green lines in Fig. 7*E* (*Inset*) show the locations of the interior channel walls from the fiber into the FTW. Although there is a small step change in channel dimension at the fiber–FTW interface, we found that smooth streamlines were maintained at this transitionary region during device operation (Movie S2).

We flowed live and dead BA/F3 cells suspended in a low-conductivity isoosmotic solution through a 75-cm-long inertial-DEP cell separation device with the FTW coupler at a rate of 100 μL min^{-1}. Under an applied field at 10 MHz, time-averaged LEF streak images in Fig. 8 show that physical partitioning of the live BA/F3 cells (*Left*) and dead BA/F3 cells (*Right*) in flow is maintained through the fiber–FTW interface. In the absence of applied voltage, both the live and dead cells undergo migration dictated by the inertial focusing forces, and are localized to the outer outlets. When the applied voltage is increased to 30 V, live cells are localized to the center outlet while dead cells are localized to the outer two prongs. We note that the cluster of cells seen near the fiber–FTW interface in the live BA/F3 cell separation at 30 V is a result of some trapped cells at the fiber–FTW interface and does not disrupt the cell streamline. A movie of real-time particle flow of live cells within the FTW chip as voltage is varied can be found in *SI Appendix* (Movie S3).

Cell populations obtained from each outlet prong were analyzed using flow cytometry after flowing through the device under a 30-V applied voltage. We found that 98% of dead cells were localized to the right and left outlets, while 85% of live cells were localized to the center channel (Fig. 8*C*).

Discussion

We introduce fiber microfluidics, a fiber-based platform for fabricating complex microfluidic devices. Fibers are produced using the thermal drawing process, in which intricate geometries patterned into preforms at the millimeter scale are dimensionally reduced to the microscale. Microfluidic channels realized through this process offer many distinct advantages. First, microchannels can be fabricated with complete design control over cross-sectional geometric shape. We have utilized the cross-sectional geometric tunability of the fiber microfluidics platform to study inertial microfluidics in channels with concave cross-sections that are inaccessible through planar fabrication techniques. The agreement between theory and experiment established in this study enables "velocity sculpting," in which custom tailoring of inertial equilibrium positions by modification of channel geometry enables future exploration of inertial microfluidic physics and next-generation particle separation devices. Second, fiber microfluidics are compatible with a wide range of materials, such as transparent insulators, conducting polymers, and metals, allowing precise placement of functional components at any location abutting channel walls. We demonstrate this multimaterial functionality by incorporating conductive materials along the surface of a crescent-shaped channel with geometric placement optimized for inertial-DEP cell separation. The resulting device performs sheathless separation of live and dead BA/F3 cells at the device outlet at high throughput (100 μL min^{-1}) using a 3D-printed FTW mating chip that is able to split flow streams out of the fiber without disturbing laminar flow. Third, fiber microfluidics can be produced at hundreds-meter lengths under a single draw, allowing for longer interaction lengths and facilitating production at scale.

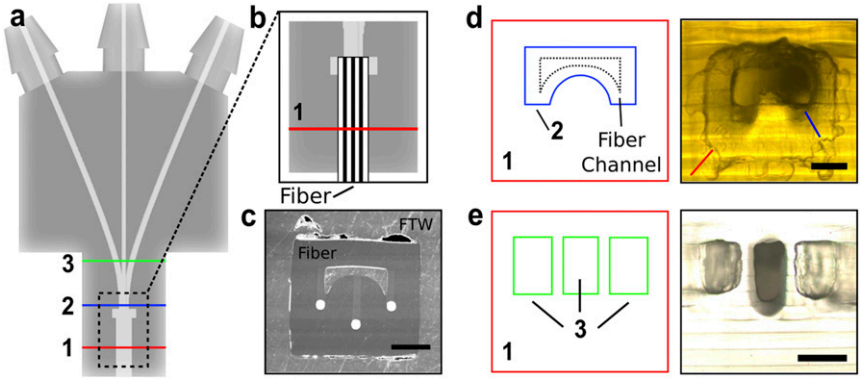

Fig. 6. FTW chip design. (*A*) A top-down schematic of the FTW chip showing cutlines that run through (*1*) the self-aligning port, (*2*) the fiber/FTW interface, and (*3*) the trifurcation fork. (*B*) Graphic showing a top-down view of how the fiber interfaces with the FTW chip. (*C*) Cross-sectional SEM image of the fiber inserted into the FTW chip along cutline *1*. (*D*, *Left*) Cross-sectional geometry of the FTW chip along cutline *2* (blue), with the relative position of the fiber port (red). The black dotted line represents the geometry and location of a half-bowtie fiber if correctly slotted into the self-aligning port. (*D*, *Right*) A cross-sectional optical image of the FTW chip at cutline *2*. The blue arrow points to the geometry at cutline *2*, and the red arrow to the geometry at cutline *1*. (*E*, *Left*) Cross-sectional geometry of the trifurcation fork at cutline *3* (green) with its relative location to the fiber port (red). (*E*, *Right*) Cross-sectional image of FTW chip at cutline *3*. (All scale bars: 200 μm.)

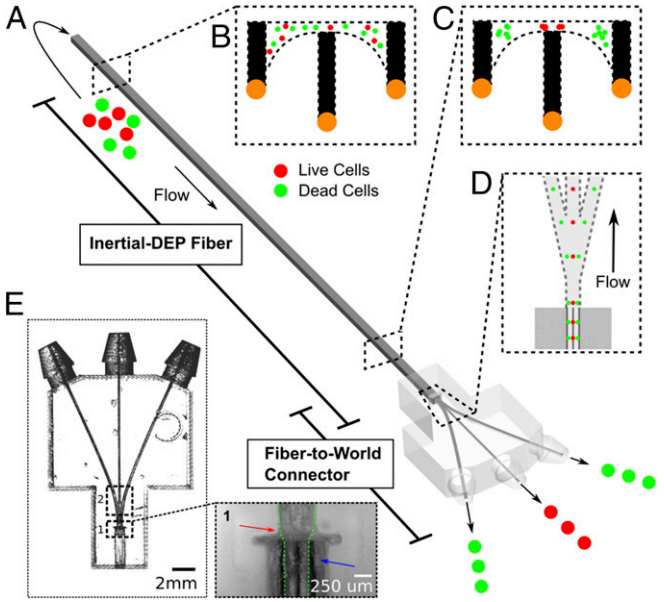

Fig. 7. Inertial-DEP fiber cell separation device design and characterization. (*A*) Schematic of a complete cell separation fiber device with FTW connection. (*B*) Two types of particles enter the device at the fiber inlet in a random distribution. (*C*) Particles are spatially separated within the fiber channels by transverse forces. In this case, green weak-DEP particles are partitioned to the outside edges of channel, while red pDEP particles are guided to the center of the channel. (*D*) Laminar flow is maintained at the fiber–FTW interface, allowing unlike particles to be physically separated by a stream-splitting trifurcation fork. (*E*) Image of a 3D-printed FTW connector showing the two sections of the chip: (*1*) the self-aligning mating port, (*2*) the stream splitting trifurcation fork (*Inset*) Image of the Inertial-DEP fiber (blue arrow) mated with the FTW internal interface (red arrow). The green line shows the combined channel outline.

As a stand-alone fiber, fiber microfluidics is well-suited for applications that would be enhanced by increased control of channel cross-sectional geometry and where the longer channels allow for increased interaction time. However, in applications that require channel splitting, such as mixing or separations, or variations in cross-sectional area, the axially symmetric geometry of stand-alone fibers may limit their effectiveness. Some of these limitations can be at least somewhat mitigated. For example, it is possible to introduce axial asymmetry to the fiber during the draw process, such as by using a nonuniform preform or by real-time adjustment of draw speeds, to introduce channel splitting or modify the cross-sectional shape along the fiber. More importantly, we envision that fiber microfluidics will be used as a component of integrated microfluidic systems that leverage the features of both fibers and conventional planar microfluidic designs. Optimization of coupling methods to traditional microfluidic devices manufactured using microfabrication or soft lithography similar to that shown for the FTW mating chip will be imperative to the development of integrated fiber and planar devices with complementing functionality.

In summary, we have developed a microfluidics fabrication approach designed to address many disadvantages inherent to conventional planar microfabrication techniques, which are restricted in their ability to create microchannels with arbitrary cross-sections, precisely placed electrodes, and sizes larger than that of the underlying silicon wafer. Unrestricted control over channel geometry will allow for direct applications in microdroplet formation and microfluidic hydrogel fabrication, in which channel geometry plays a large role in shaping microstructures. Furthermore, in conjunction with its multimaterial functionality, fiber microfluidics will open opportunities to shape hydrodynamic flows and electric fields for applications in cell separations, electrowetting, and electrotaxis. Finally, the fiber form factor lends itself to applications that require long interaction lengths, such as molecular separations, and biomimicry of high-aspect-ratio structures such as blood capillaries

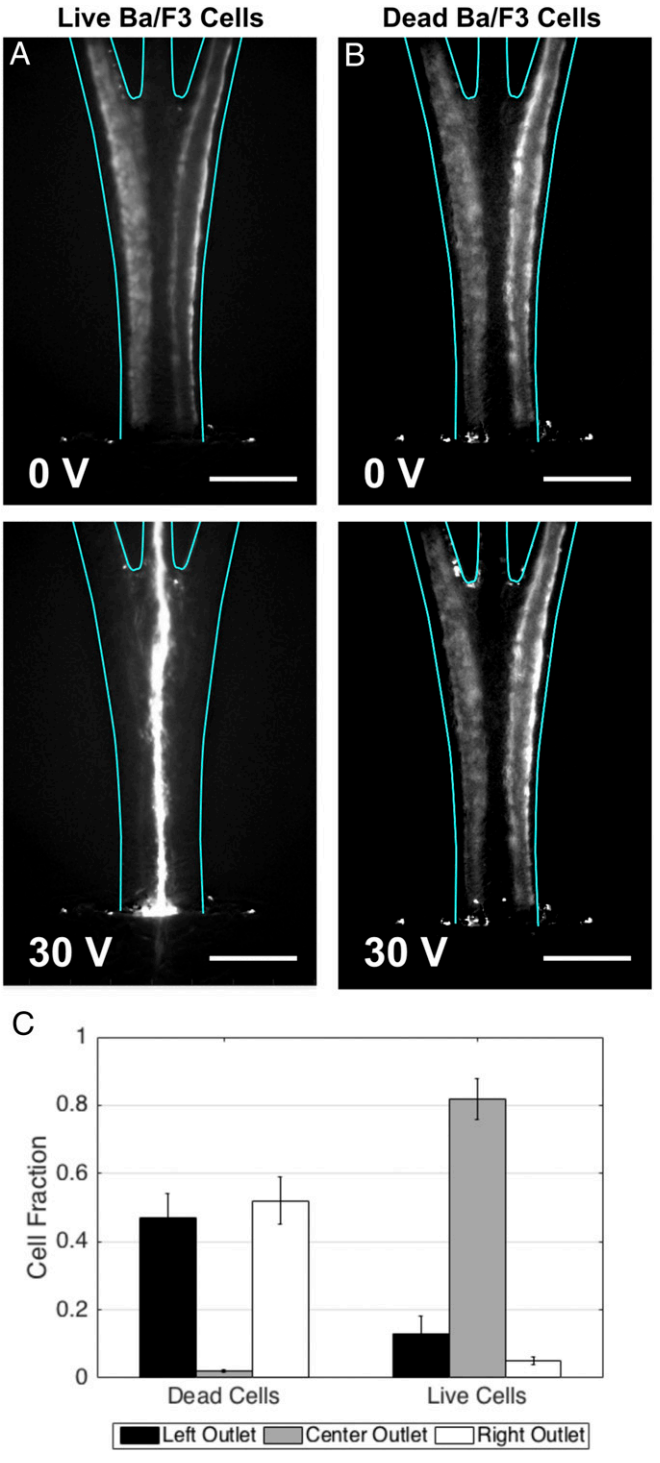

Fig. 8. Live/dead cell separation in the inertial-DEP fiber device. LEF images of (*A*) live cell and (*B*) dead cell solutions flowed through the complete inertial-DEP fiber device at various values for applied voltage. Images were taken between the fiber–FTW interface and the trifurcation fork within the FTW coupler. (Scale bar: 500 μm.) (*C*) Distribution of live and dead cells out of the left, center, and right outlets, measured via flow cytometry.

and vascular transport tissues. Ultimately, we envision a future in which the unique capabilities of the fiber microfluidic platform make it a common tool, alongside existing methods such as microfabrication, soft lithography, and 3D printing, for microfluidic device engineers to optimally address their application needs.

Experimental

Fiber Fabrication. The equilateral cross-fiber, cross-shaped fibers were made out of polycarbonate (McMaster-Carr) and annealed at 180 °C in a hot press. To fabricate the star fiber, we used wire electrical discharge machining (wire EDM) to fabricate an aluminum rod with a star-shaped cross-section (XACT Wire EDM Corp.). The star-shaped aluminum rod was coated with a spray-on and heat-cured Teflon coating (Durafilm Teflon Black; applied by American Durafilm Co. Inc.). The inserts were removed, and the preform was drawn using the thermal fiber drawing technique at 240 °C. The distance between opposite points of the star channel was 150 μm. Particles were observed in the $+y$ direction for both the star- and cross-shaped channels. Fluidic connections to the fibers were made by inserting them into 0.004-in.-inner-diameter polyetheretherketone PEEK tubing (IDEX Health and Science) and sealing with epoxy.

The inertial-DEP fiber was fabricated with a COC (TOPAS; Grade 8007) cladding and CPE (Hillas Packaging) electrodes. The CPE used is a proprietary blend comprised of a low-density polyethylene matrix impregnated with carbon black. It was codrawn with 50-μm copper wire (Sigma Aldrich). Electrodes were connected to the fiber by mechanically exposing the electrode of the fiber at the desired position and connecting it to an external wire using conductive silver paint (Ted Pella Inc.). Fluidic connections were made in the same manner as the inertial focusing fibers.

Confocal Imaging. Fiber samples were mounted to a glass slide using epoxy. Flow was directed into the fibers in the same manner as the LEF experiments. To prevent image distortion from rough fiber surfaces or index mismatch, the fibers were observed through immersion oil (n = 1.515; Olympus Corp.). Confocal imaging on the inertial focusing fibers was performed by using a confocal laser scanning microscope (FluoView FV1000; Olympus Corporation) to scan a 3D section of the fiber channel with an exposure time of 200 μs per pixel. Particle distributions were obtained by taking the projection of the 3D section onto the x-y plane.

DEP Cell Separation Device Fabrication and Operation. The FTW connector was printed using a high-resolution stereolithographic 3D printer (Projet 6000 HD; 3D Systems) with a clear resin (Visijet SL Clear). The channels were primed with a BSA solution (1× PBS/3% BSA) at a flow rate of 50 μL min^{-1} for 30 min. To control the flow rates out of each outlet of the FTW connector, the two outer prongs of the outlet ports of the FTW connector were connected to syringe pumps that withdrew fluid at a controlled flow rate of 40 μL min^{-1}. Because the inlet flow rate of the device was 100 μL min^{-1}, this set the center outlet flow rate to 20 μL min^{-1}.

Particle Preparation for In-Fiber Visualizations. We used 10-μm green fluorescent polystyrene particles with carboxylate surface groups (Polysciences, Inc). The particles were dispersed in deionized water at a concentration of 100,000 particles mL^{-1}. For in-fiber visualizations, live BA/F3 cells were stained with a 1-μM Calcein Red/Orange (CellTrace, Life Technologies) and dead BA/F3 cells were stained with a 1-μM Calcein AM (CellTrace, Life Technologies) PBS solution. The stained cells were recentrifuged and resuspended in a low-conductivity media (8.5 wt % sucrose, 0.3 wt % dextrose) to a concentration of ~1 million cells mL^{-1} and flowed through a 35-μm syringe filter (BD Biosciences) to remove cell debris.

Flow Cytometry. Live and dead particles were stained with a 1-μM Calcein AM (CellTrace, Life Technologies) PBS solution, with concentrations of 50,000 and 300,000 cells mL^{-1}, respectively. Cells collected at each outlet were then analyzed using a flow cytometer (Accuri C6).

LEF Microscopy. Flow was delivered to the fibers using a syringe pump (Fusion 200; Chemyx) using syringes connected to the fiber-interfacing tubing. Particles were observed through the glass coverslip using an optical microscope (Zeiss AXIO), a CCD camera (Imager QE, LaVision), and fluorescence light source (X-Cite 120; EXFO).

ACKNOWLEDGMENTS. The authors are grateful to P. Anikeeva for help with confocal microscopy experiments, S. Johnson and F. Wang for help with numerical simulations, and S. Kooi and M. Tarkanian for assistance with equipment. R.Y., E.L., T.K., and Y.F. were supported in part by the National Science Foundation under the Center for Materials Science and Engineering (DMR-0819762 and DMR-1419807) and the US Army Research Laboratory and the US Army Research Office through the Institute for Soldier Nanotechnologies under Contract W911NF-13-D-0001 and the National Institutes of Health under Contract 1R21EB022729. J.L., H.-W.S., and J.V. were supported in part by the Defense Advanced Research Projects Agency under Contract N66001-11-1-4182 and the National Institutes of Health under Contract 1U24AI118656 and 1R21EB022729. J.L. was supported by the Korea Foundation for Advanced Studies Fellowship.

1. Beebe DJ, Mensing GA, Walker GM (2002) Physics and applications of microfluidics in biology. *Annu Rev Biomed Eng* 4:261–286.
2. Mark D, Haeberle S, Roth G, von Stetten F, Zengerle R (2010) Microfluidic lab-on-a-chip platforms: Requirements, characteristics and applications. *Chem Soc Rev* 39: 1153–1182.
3. Elvira KS, Casadevall i Solvas X, Wootton RCR, deMello AJ (2013) The past, present and potential for microfluidic reactor technology in chemical synthesis. *Nat Chem* 5: 905–915.
4. Nguyen NT, Wereley S (2006) *Fundamentals and Applications of Microfluidics* (Artech House, Boston).
5. Dittrich PS, Manz A (2006) Lab-on-a-chip: Microfluidics in drug discovery. *Nat Rev Drug Discov* 5:210–218.
6. Iliescu C, Taylor H, Avram M, Miao J, Franssila S (2012) A practical guide for the fabrication of microfluidic devices using glass and silicon. *Biomicrofluidics* 6: 16505–1650516.
7. Duffy DC, McDonald JC, Schueller OJA, Whitesides GM (1998) Rapid prototyping of microfluidic systems in poly(dimethylsiloxane). *Anal Chem* 70:4974–4984.
8. Mair DA, Geiger E, Pisano AP, Fréchet JMJ, Svec F (2006) Injection molded microfluidic chips featuring integrated interconnects. *Lab Chip* 6:1346–1354.
9. Yan S, et al. (2014) On-chip high-throughput manipulation of particles in a dielectrophoresis-active hydrophoretic focuser. *Sci Rep* 4:5060.
10. Voldman J (2006) Electrical forces for microscale cell manipulation. *Annu Rev Biomed Eng* 8:425–454.
11. Kim U, et al. (2007) Selection of mammalian cells based on their cell-cycle phase using dielectrophoresis. *Proc Natl Acad Sci USA* 104:20708–20712.
12. Park J, et al. (2010) Simple haptotactic gradient generation within a triangular microfluidic channel. *Lab Chip* 10:2130–2138.
13. Cheng I-F, et al. (2015) Antibody-free isolation of rare cancer cells from blood based on 3D lateral dielectrophoresis. *Lab Chip* 15:2950–2959.
14. Wu L, Guan G, Hou HW, Bhagat AAS, Han J (2012) Separation of leukocytes from blood using spiral channel with trapezoid cross-section. *Anal Chem* 84: 9324–9331.
15. Kim J, et al. (2016) Inertial focusing in non-rectangular cross-section microchannels and manipulation of accessible focusing position. *Lab Chip* 16:992–1001.
16. Warkiani ME, et al. (2014) Slanted spiral microfluidics for the ultra-fast, label-free isolation of circulating tumor cells. *Lab Chip* 14:128–137.
17. Amini H, Lee W, Di Carlo D (2014) Inertial microfluidic physics. *Lab Chip* 14:2739–2761.
18. Di Carlo D, Edd JF, Humphry KJ, Stone HA, Toner M (2009) Particle segregation and dynamics in confined flows. *Phys Rev Lett* 102:094503.
19. Liu C, Hu G, Jiang X, Sun J (2015) Inertial focusing of spherical particles in rectangular microchannels over a wide range of Reynolds numbers. *Lab Chip* 15: 1168–1177.
20. Bhagat AAS, Kuntaegowdanahalli SS, Kaval N, Seliskar CJ, Papautsky I (2010) Inertial microfluidics for sheath-less high-throughput flow cytometry. *Biomed Microdevices* 12:187–195.
21. Hur SC, Tse HTK, Di Carlo D (2010) Sheathless inertial cell ordering for extreme throughput flow cytometry. *Lab Chip* 10:274–280.
22. Tanaka T, et al. (2012) Separation of cancer cells from a red blood cell suspension using inertial force. *Lab Chip* 12:4336–4343.
23. Tanaka T, et al. (2012) Inertial migration of cancer cells in blood flow in microchannels. *Biomed Microdevices* 14:25–33.
24. Gossett DR, et al. (2012) Inertial manipulation and transfer of microparticles across laminar fluid streams. *Small* 8:2757–2764.
25. Segre G, Silberberg A (1962) Behaviour of macroscopic rigid spheres in Poiseuille flow. *J Fluid Mech* 14:115–135.
26. Ho BP, Leal LG (1974) Inertial migration of rigid spheres in two-dimensional unidirectional flows. *J Fluid Mech* 65:365–400.
27. Yang J, et al. (1999) Dielectric properties of human leukocyte subpopulations determined by electrorotation as a cell separation criterion. *Biophys J* 76:3307–3314.
28. Wei MT, Junio J, Ou-Yang HD (2009) Direct measurements of the frequency-dependent dielectrophoresis force. *Biomicrofluidics* 3:12003.
29. Su H-W, Prieto JL, Voldman J (2013) Rapid dielectrophoretic characterization of single cells using the dielectrophoretic spring. *Lab Chip* 13:4109–4117.
30. Moon H-S, et al. (2011) Continuous separation of breast cancer cells from blood samples using multi-orifice flow fractionation (MOFF) and dielectrophoresis (DEP). *Lab Chip* 11:1118–1125.
31. Shafiee H, Sano MB, Henslee EA, Caldwell JL, Davalos RV (2010) Selective isolation of live/dead cells using contactless dielectrophoresis (cDEP). *Lab Chip* 10:438–445.

32. Alazzam A, Stiharu I, Bhat R, Meguerditchian AN (2011) Interdigitated comb-like electrodes for continuous separation of malignant cells from blood using dielectrophoresis. *Electrophoresis* 32:1327–1336.
33. Vahey MD, Voldman J (2008) An equilibrium method for continuous-flow cell sorting using dielectrophoresis. *Anal Chem* 80:3135–3143.
34. Huang Y, Hölzel R, Pethig R, Wang XB (1992) Differences in the AC electrodynamics of viable and non-viable yeast cells determined through combined dielectrophoresis and electrorotation studies. *Phys Med Biol* 37:1499–1517.
35. Cheng IF, Chang HC, Hou D, Chang HC (2007) An integrated dielectrophoretic chip for continuous bioparticle filtering, focusing, sorting, trapping, and detecting. *Biomicrofluidics* 1:21503.
36. Alshareef M, et al. (2013) Separation of tumor cells with dielectrophoresis-based microfluidic chip. *Biomicrofluidics* 7:11803.
37. Jia Y, Ren Y, Jiang H (2015) Continuous dielectrophoretic particle separation using a microfluidic device with 3D electrodes and vaulted obstacles. *Electrophoresis* 36: 1744–1753.
38. Gumennik A, et al. (2012) All-in-fiber chemical sensing. *Adv Mater* 24:6005–6009.
39. Bayindir M, et al. (2004) Metal-insulator-semiconductor optoelectronic fibres. *Nature* 431:826–829.
40. Chocat N, et al. (2012) Piezoelectric fibers for conformal acoustics. *Adv Mater* 24: 5327–5332.
41. Egusa S, et al. (2010) Multimaterial piezoelectric fibres. *Nat Mater* 9:643–648.